Measurements and Predictions of a Highly Turbulent Flowfield in a Turbine Vane Passage

R. W. Radomsky[1]

K. A. Thole
e-mail: thole@vt.edu

Mechanical Engineering Department,
Virginia Polytechnic Institute and State University,
Blacksburg, VA 24061-0238

As highly turbulent flow passes through downstream airfoil passages in a gas turbine engine, it is subjected to a complex geometry designed to accelerate and turn the flow. This acceleration and streamline curvature subject the turbulent flow to high mean flow strains. This paper presents both experimental measurements and computational predictions for highly turbulent flow as it progresses through a passage of a gas turbine stator vane. Three-component velocity fields at the vane midspan were measured for inlet turbulence levels of 0.6%, 10%, and 19.5%. The turbulent kinetic energy increased through the passage by 130% for the 10% inlet turbulence and, because the dissipation rate was higher for the 19.5% inlet turbulence, the turbulent kinetic energy increased by only 31%. With a mean flow acceleration of five through the passage, the exiting local turbulence levels were 3% and 6% for the respective 10% and 19.5% inlet turbulence levels. Computational RANS predictions were compared with the measurements using four different turbulence models including the k-ε, Renormalization Group (RNG) k-ε, realizable k-ε, and Reynolds stress model. The results indicate that the predictions using the Reynolds stress model most closely agreed with the measurements as compared with the other turbulence models with better agreement for the 10% case than the 19.5% case.
[S0098-2202(00)00804-X]

Introduction

As highly turbulent flow exiting the combustor of a gas turbine engine passes through a downstream airfoil passage, this flow experiences high rates of strain as a result of acceleration and streamline curvature. Airfoil surface heat transfer measurements, particularly on the pressure side, have local convection coefficients for a highly turbulent flow as much as two times that for low turbulence conditions (Ames [1] and Radomsky and Thole [2]). One of the goals for the turbine industry is to predict heat loads on the turbine airfoils through the use of either a boundary layer or a full Reynolds-averaged Navier-Stokes (RANS) code. Prior to making boundary layer and, ultimately, heat transfer predictions, it should be proven that the core flow inside the passage can be accurately predicted since it would provide an external boundary condition for the boundary layer calculations.

Although predicting these turbulence levels might be thought of as a first step, there is a lack of experimental data used for verifying these computational predictions. This scarceness in quality benchmark data is particularly evident at turbulence levels relevant to those exiting a gas turbine combustor, which can be as high as 20 to 30% (Goldstein et al. [3]). This paper presents both experimental measurements and computational predictions of a highly turbulent flow convecting through a turbine vane passage at inlet turbulence levels of 0.6%, 10%, and 19.5%. In the passage the flow encounters strong streamline curvature and an acceleration where the exit velocities are five times faster than the inlet velocities. The experimental measurements include all three components of mean and fluctuating velocity quantities measured with a laser Doppler velocimeter. RANS calculations were completed using four different turbulence models including the following: standard k-ε, RNG k-ε, realizable k-ε, and Reynolds stress model.

[1]Current address: United Technologies Research Center, 411 Silver Lane, East Hartford, CT 06108.

Contributed by the Fluids Engineering Division for publication in the JOURNAL OF FLUIDS ENGINEERING. Manuscript received by the Fluids Engineering Division August 30, 1999; revised manuscript received July 10, 2000. Associate Technical Editor: P. Bearman.

Past Studies

The effect of streamline curvature on the structure of the turbulent boundary layer flows was extensively discussed in a review by Bradshaw [4]. In this discussion, Bradshaw noted that eddy viscosity models tend to underestimate the effects of the secondary strain on the Reynolds stresses since the coefficients of the primary and secondary strains are modeled to be equal. Bradshaw [4] noted that extra rates of strain, such as streamline curvature, had a large impact on the Reynolds stresses and suggested that a multiplier of ten be placed in front of the extra strain rate term to account for the increased turbulent stress.

Launder et al. [5] performed an analysis on a boundary layer flow over a curved surface using a full Reynolds stress closure model. By combining the effects of the generation as well as the pressure-strain effects Launder et al. [5] showed an eight fold amplification of the secondary strain term, which is close to the multiplier of ten suggested by Bradshaw [4]. Their analysis suggests that the full Reynolds stress closure models give a better representation of the effects of extra rates of strain, such as streamline curvature.

Durban and Speziale [6] examined the assumption of local isotropy in the presence of mean strain. Analysis of the transport equation for the dissipation tensor showed that for the local isotropy to be a valid assumption, the ratio of the turbulent time scales to the mean rate of strain should be small, $Sk/\varepsilon \ll 1$. This ratio is rarely satisfied for many applications and particularly for turbomachinery flows where both high levels of turbulence and streamline curvature are present.

Lakshminarayana's [7] review on computation of turbomachinery flows is in agreement with the above discussion in that for flows with high streamline curvature a full Reynolds stress closure model should give improved results over two-equation k-ε models. Lakshminarayana [7] suggested that the isotropic assumptions in the two-equation models do not allow accurate flowfield predictions when there is streamline curvature. Lou and Lakshminarayana [8] predicted the effects of streamline curvature on wall turbulence for flow in 90 and 180 deg ducts. Their results showed the standard k-ε model failed to predict the damping of the turbu-

lence near the convex wall and failed to predict the enhancement of the turbulence near the concave wall. The Reynolds stress model, with the standard transport equation for dissipation, was able to predict the suppression of the turbulence near the convex wall but still somewhat underestimated the increased turbulence near the concave wall.

With respect to streamline curvature, flow through a turbine vane passage can be compared to that through a curved duct. The difference between these two flows, however, is that there is an added strain due to the flow acceleration through the passage in the case of a turbine vane. Another difference is that higher inlet turbulence levels are being considered for the turbine vane case as compared to those in curved wall simulations. These differences warrant an evaluation of the various turbulence models for high turbulence flows through a turbine vane passage.

Experimental Facility and Instrumentation

For these studies, a first stage gas turbine vane geometry was scaled up by a factor of nine to allow for high measurement resolution. The vane test section is shown schematically in Fig. 1. Although the inlet Reynolds number was matched for the engine operating at altitude conditions, the Mach number was not matched. Prior to predicting the more complicated case of compressible flow, however, assessing turbulence models at incompressible conditions is needed.

The construction and development of the scaled-up stator vane test section have been previously documented by Kang et al. [9], Kang and Thole [10] and Radomsky and Thole [11]. The test section consists of a central vane with leading edges of two adjacent vanes to give two vane passages. The initial portion of the outer sidewall exactly matches the profile of an adjacent vane. At the point where an adjacent vane geometry stops for the outer vane, the flexible wall was positioned such that the pressure distribution on the central vane matched an inviscid pressure distribution numerically predicted for a two-dimensional periodic cascade at low-speed conditions. As will be shown later in this paper, tailboards and sidewall bleeds insured periodic flow in the two passages surrounding the central vane. The thickness of each endwall boundary layer at one chord upstream of the vane was 9% of the total span. A description of the turbine vane geometry and operating conditions is given in Table 1.

An active-grid turbulence generator, described in detail by Bangert et al. [12], was placed at 1.9 chords upstream of the vane stagnation. The turbulence generator used high velocity jets blowing in both the upstream and downstream directions to generate turbulence levels between 10% and 20% measured at 0.33 chords upstream of the vane stagnation location. The integral length scale

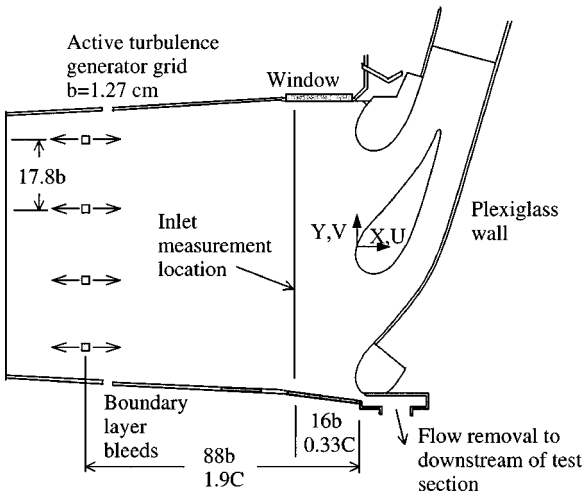

Fig. 1 Schematic of stator vane test section

Table 1 Geometrical and flow conditions for the stator vane geometry

Scaling factor	9
Scaled-up chord length	59.4 cm
Pitch / chord	0.77
Span / chord	0.93
Re_{in}	2.30×10^5
Inlet and exit angles	0° and 78°

at 0.33 chords upstream for the 10% and 20% cases were $\Lambda_x/P = 0.11$ and 0.12, respectively, and were uniform across the span to within 4%.

For the results reported in this paper, the velocity field measurements were taken at the vane mid-span from mid-pitch to mid-pitch around the central vane. A Cartesian coordinate system, with the origin at the flow stagnation point, as shown in Fig. 1, was maintained for all measurements. Flowfield measurements, which included all three velocity components and rms velocities, were made with a two-component laser Doppler velocimeter (LDV) with digital burst correlator processors. For the 0.6% freestream turbulence experiments, 10,000 data points were taken for the mean and rms statistics. For the 10% and 19.5% freestream turbulence experiments, 25,000 data points taken in coincidence mode were averaged to determine the mean, rms values, and Reynolds shear stress. The measured velocities were corrected for bias errors using the residence time weighting correction scheme. Autocorrelation length scales were measured with a single sensor hot-wire having a length of 1.5 mm, and diameter of 4 microns. A complete description of the measurement techniques is given in Radomsky and Thole [11].

The uncertainty estimates were made using the procedures outlined by Moffat [13]. The precision uncertainties for the 10% and 20% inlet turbulence levels were estimated using a 95% confidence interval. The precision uncertainty for the mean velocities was 0.8% for both the 10% and 20% turbulence levels while the bias uncertainty for both was estimated to be 1%. The precision uncertainty for the rms of the velocity fluctuations was 2.0% for the 20% inlet turbulence case while the uncertainties in the measured Reynolds shear stress was estimated to be 12%. The precision uncertainty for the rms of the velocity fluctuations was 2.2% for the 10% inlet turbulence case while the uncertainties in the measured Reynolds shear stress was estimated to be 11%. For the hot-wire measurements, the precision uncertainty for the 20% case for the mean and rms velocities were 3.5% and 4.8%, respectively, while the uncertainty in the integral length scale was estimated to be 12.4%.

Computational Methods and Turbulence Models

The RANS calculations were performed using a pressure-based flow solver whereby the pressure and velocity are coupled using the Semi-Implicit Method for Pressure-Linked Equations (SIMPLE) algorithm (Patankar [14]). Second-order discretization was used for the turbulence and RANS equations. The solver chosen for this study was from the commercial package FLUENT/UNS (FLUENT 5 [15]) providing solution adaptive grid capabilities and offered a number of different turbulence models for comparisons.

The two-dimensional computational domain used in this investigation is illustrated in Fig. 2. The inlet boundary condition was placed one chord length upstream of the vane stagnation where the incoming velocity field is unaffected by the presence of the vane. The outlet boundary location, determined through a number of CFD studies to insure that the location did not affect the calculations, was placed at one and a half chord lengths downstream of the trailing edge of the vane. Periodic boundary conditions, whereby the domain was split at the flow stagnation location, were used everywhere except for the inlet, outlet, and vane sur-

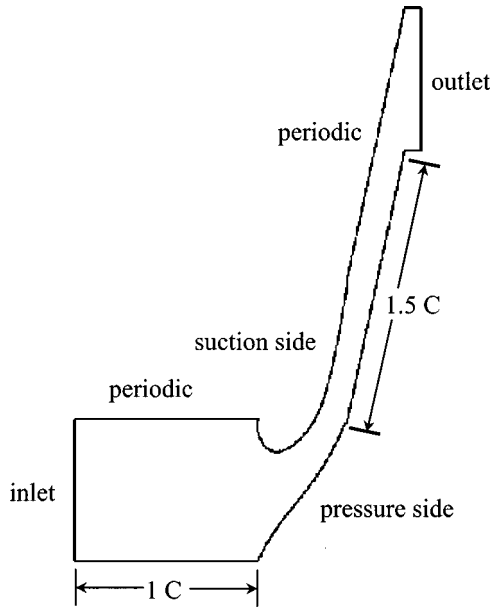

Fig. 2 Computational domain modeling a single passage of a vane cascade

face. The inlet boundary condition was set to a uniform velocity to match the turbine inlet Reynolds number given in Table 1. The boundary condition at the exit was specified as an outflow boundary condition, which assumes that the flow gradients are small. A no-slip boundary condition was imposed at the vane surface.

A hybrid-meshing scheme, available in GAMBIT (FLUENT 5, Inc., 1998) was used in which quadrilateral cells were placed near the surface of the vane and tetrahedral cells were used in the freestream region. The near-wall region, which was not the focus of this study, was modeled in all of the stator vane simulations using non-equilibrium wall functions given by Kim and Choudhury [16]. The near-wall cell was located between $30 < y^+ < 60$ to insure proper usage of the wall functions. A grid sensitivity study was performed in which a series of increasingly finer meshes were examined. Figure 3 shows the normalized total velocity, $|U|/U_{\text{inlet}}$, and turbulent kinetic energy, k/U_{inlet^2}, at a location just downstream of the flow stagnation location at $X/P = 0.06$ for grid sizes ranging in size from 12,000 to 154,000. Very little difference is observed in either the total velocity or turbulent kinetic energy for the cases with greater than 31,000 cells. The results presented in this paper for all the turbulence models are for the larger mesh with 154,000 cells. Convergence for the cases presented in this paper was typically achieved after 6000 iterations. Numerical uncertainty, in terms of the convergence criteria, was assessed by comparing the lift coefficient for what was considered to be a converged case and comparing that with a case with more iterations. The lift coefficient was determined by integrating the vertical force around the airfoil. The difference in lift coefficients between these two cases was 0.07% for over 600 iterations.

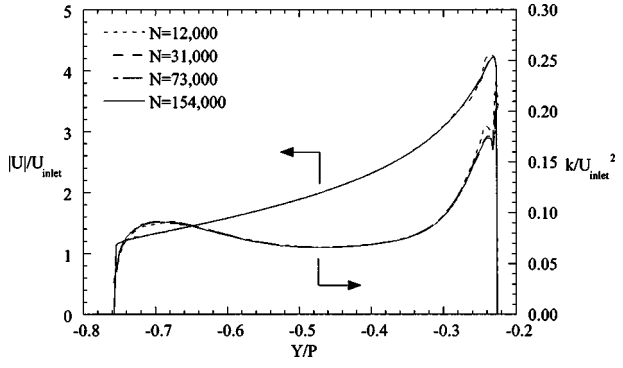

Fig. 3 Normalized total velocity, $|U|/U_{\text{inlet}}$, and turbulent kinetic energy, k/U^2_{inlet}, for different grid sizes at $X/P=0.06$ for the 19.5% case

As discussed earlier, several turbulence models were compared for predicting the high turbulence convecting through the turbine vane passage. The turbulence models used were the k-ε model (Launder and Spalding [17]), RNG k-ε model (Yahkot et al. [18]), realizable k-ε model (Shih et al. [19]), and the Reynolds stress model (Launder et al. [5]).

The standard k-ε, RNG k-ε, and realizable k-ε models are similar in that the models use an eddy viscosity and mean velocity gradients to calculate the Reynolds shear stress as in the following equation

$$-\rho\overline{u_i' u_j'} = \mu_t\left(\frac{\partial U_i}{\partial x_j} + \frac{\partial Uj}{\partial x_i}\right) - \frac{2}{3}\left(\rho k + \mu_t \frac{\partial U_i}{\partial x_j}\right)\delta_{ij} \tag{1}$$

The eddy viscosity is calculated for both the k-ε model and the RNG k-ε model at high Reynolds models using the following relation

$$\mu_t = \rho C_\mu \frac{k^2}{\varepsilon} \tag{2}$$

where C_μ is a constant value of 0.09 for the k-ε model and 0.0845 for the RNG k-ε model. Note that no changes were made to any of the model constants when using these models for the predictions presented in this paper. At low Reynolds number conditions an additional differential equation is solved for the turbulent viscosity. The difference between the k-ε and RNG k-ε model is that for the RNG k-ε model the constants were optimized to give improved performance. In addition, the RNG k-ε model has a higher order expansion term in the transport equation for the turbulent dissipation rate, defined below

$$R = \frac{C_\mu \rho \eta^3 (1 - \eta/\eta_0)}{1 + \beta \eta^3} \frac{\varepsilon^2}{k} \tag{3}$$

In Eq. (3), η is the ratio of the time scales, $\eta \equiv S\,k/\varepsilon$, previously discussed. This additional term affects the amount of destruction of dissipation in the transport equation. For small values of η, $R \rightarrow 0$, but for large values of η, η will exceed η_0, and the R term becomes negative increasing the overall dissipation rate and decreasing the turbulent viscosity. Since the Reynolds stress is computed using Eq. (1), it should then be expected that in regions of high strain rates the RNG k-ε model would predict lower Reynolds stresses than would the k-ε model.

The realizable k-ε model used in this study, developed by Shih et al. [19] also calculates the Reynolds shear stress based on a turbulent viscosity and the mean velocity gradients. The difference for this model is that there are imposed constraints such that the normal stress is always positive ($\overline{u'^2} > 0$) and that the Schwarz inequality is not violated. From Eq. (1) it can be easily seen that when a large strain rate occurs a negative normal stress can result. To satisfy these constraints, a variable form of C_μ that is a function of the mean strain rate, turbulent kinetic energy and dissipation rate was developed. Shih et al. [19] also used a different form of the dissipation equation that was developed from the dynamic equation of the mean-square vorticity fluctuation at large turbulent Reynolds numbers. In this formulation, the production of dissipation is proportional to the mean rate of strain. The form of the dissipation transport equation used in the realizable k-ε model is thought to provide a better representation of the spectral energy transfer.

The Reynolds stress model used in this study is in the form given by Launder et al. [5]. To reduce numerical instabilities, the turbulent diffusion term, D_{ij}^T, was modeled following the sugges-

tion of Lien and Leschziner [20]. The pressure strain term was modeled using a second order technique suggested by Speziale et al. [21] since it was suggested to be more accurate for streamline curvature flows. The final term requiring modeling is the dissipation tensor, which is modeled assuming the dissipative motion is isotropic. The dissipation transport equation used for the Reynolds stress model is the same as that used in the standard k-ε model.

Computational Benchmark in a 180 Degree Duct

As a validation of the computational code used in the present study, simulations of flow through a 180 deg duct were compared to experimental data by Monson and Seegmiller [20] at a $\mathrm{Re}_{\mathrm{inlet}} = 1 \times 10^5$. This particular benchmark served to validate the computational models for a flow having strong streamline curvature. To be consistent with the stator vane simulations, a hybrid-meshing scheme was employed. To accurately resolve the separation region near the end of the turn, however, the first grid point near the wall was located at $y^+ = 1$ and a two-layer zonal model was used (Wolfstein [23]). Note that no separation occurs for the turbine vane case. The inlet boundary condition was specified at four channel widths upstream of the turn. The inlet conditions used were tabulated mean and turbulence values reported by Monson and Seegmiller [22] from their experimental measurements. The outflow boundary condition was located twelve channel widths downstream of the end of the turn. After performing grid sensitivity studies, the resulting mesh contained 210,000 cells. Results from these simulations are shown in Figs. 4(*a*) through 4(*c*).

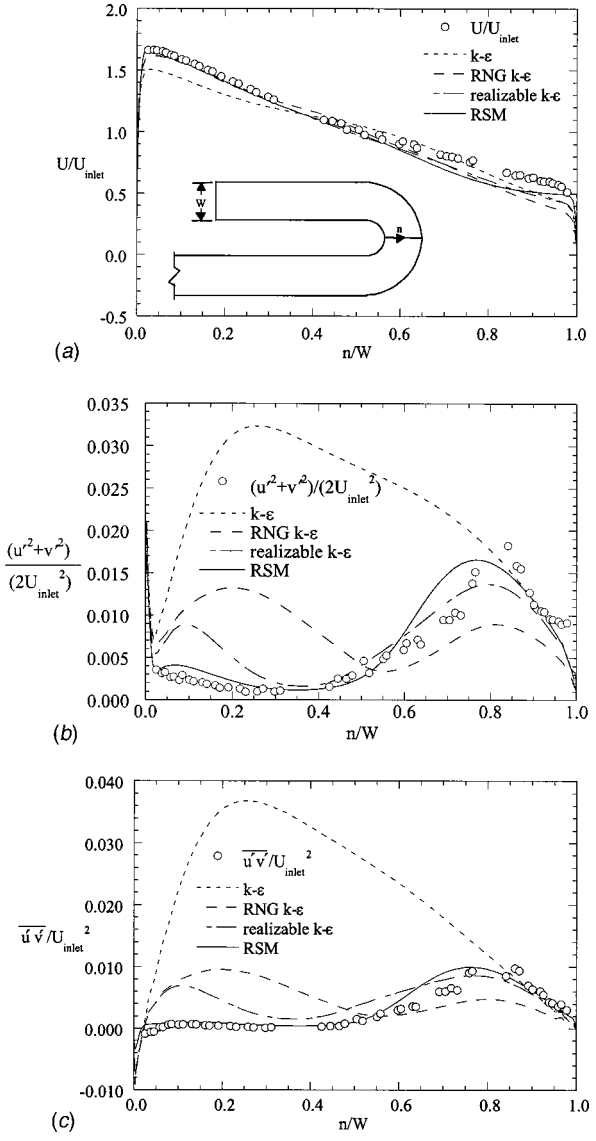

Fig. 4 (*a*) Comparison of measured and predicted streamwise velocity profiles, U/U_{inlet}, (Monson and Seegmiller [22]) at the 90 degree location in the turn; (*b*) comparison of measured and predicted normalized turbulent kinetic energy, $(u'^2+v'^2)/U_\infty^2$ (Monson and Seegmiller [22]) at the 90 degree location in the turn; (*c*) comparison of measured and predicted normalized Reynolds shear stress, $\overline{u'v'}/U_{\mathrm{inlet}}^2$ (Monson and Seegmiller [22]) at the 90 degree location in the turn

Figure 4(*a*) shows the mean component of the streamwise velocity taken at the 90 deg location, which is halfway through the turn. Note that n/W is the normal coordinate measured outward from the inner convex wall. As can be seen, with the exception of the standard k-ε model, the turbulence models are able to predict the high velocity region near the inner wall. The mean velocity near the outer wall is underpredicted by each of the turbulence models, which is similar to the results by Lou and Lakshminarayana [8] who also performed simulations on the U-duct but at a higher Reynolds number. The difference between measurements and predictions near the outer wall may be the result of three-dimensional effects in the experimental measurements that are not being modeled in these two-dimensional predictions.

Figures 4(*b*) and 4(*c*) show the measured and predicted turbulent kinetic energy and Reynolds shear stress at the 90 deg location. The standard k-ε model greatly over-predicts the magnitude of both the turbulent kinetic energy and shear stress. The RNG k-ε model fails to predict the damping of both the turbulent kinetic energy and Reynolds shear stress near the convex inner wall and underestimates the turbulence increase near the outer concave wall. The realizable k-ε model results do indicate a suppression and an increase of the turbulent kinetic energy for the convex and concave wall, respectively. As shown in other studies, the Reynolds stress model was able to accurately predict both the damping near the inner wall as well as the enhancement near the outer wall. Figures 4(*a*)–4(*c*) give validation that the code used in this study predicts results similar to that already published for flows with streamline curvature alone. The next step is to determine whether the turbulence models can adequately predict the turbulence for flow with the additional strain of flow acceleration, as in the turbine vane passage.

Inlet Conditions for the High Turbulence Turbine Vane Studies

The inlet turbulence conditions for the computations at one chord upstream were determined from measured values at one-third chord upstream (optical access for the measurements was not available at one chord). The turbulent quantities, ε and k, were set at one-chord upstream by performing trial-and-error simulations until the predicted values at one-third of a chord upstream matched the experimental measurements.

The dissipation rate was determined from measured energy spectra of the streamwise velocity fluctuations. Typical energy spectra for the streamwise fluctuations, measured at one-third chord upstream at both turbulence levels, are shown in Fig. 5 along with a comparison to the von Karman spectra and the unified relation given by Mayle et al. [24]. The measured spectra agree well with both correlations and show the existence of a well-defined inertial subrange. The inertial subrange region was used to calculate the dissipation rate by performing a curve fit to the following formula (Hinze [25] and Ames [1])

$$E_1(\kappa_1) = 1.62(18/55)\varepsilon^{2/3}\kappa_1^{-5/3} \tag{4}$$

Table 2 gives the measured and predicted turbulent kinetic energy

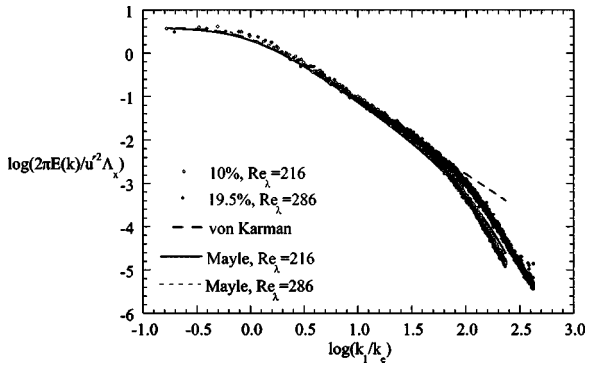

Fig. 5 Comparison of measured and predicted one-dimensional energy spectra at one-third chord upstream of the vane stagnation

values and dissipation rates at one chord ($X/C=-1$) and one-third chord. ($X/C=-0.33$) upstream of the vane for both 10% and 19.5% inlet turbulence levels.

To determine the turbulent kinetic energy (k), measurements were taken across the entire pitch of the two flow passages surrounding the central vane. Figure 6(a) shows the normalized rms levels of the streamwise (u'/U_{inlet}), cross-stream (v'/U_{inlet}), and the spanwise (w'/U_{inlet}) velocity fluctuations as well as the normalized turbulent kinetic energy measured at one-third chord upstream of the vane stagnation for the high turbulence case. The average turbulence level at this location is 19.5%. All three rms levels are close to the same value with only slightly lower spanwise fluctuations, w'/U_{inlet}. The maximum deviations relative to the average for the streamwise, cross-stream, and spanwise fluctuations were 7.5%, 10%, and 6.9%, respectively. The maximum deviation of the streamwise rms velocities to the average value across the vertical span of the turbine vane was 2.8% for the 19.5% case. Figure 6(a) also illustrates that the rms levels of the streamwise fluctuations measured using a hot-wire agree well with the LDV measurements. The turbulent kinetic energy levels given as the inlet boundary conditions at one chord upstream for all of the turbulence models are reported in Table 2. Figure 6(a) shows that for the given ε and k value at one chord upstream, the predicted k value for all of the models agrees with that measured at 0.33 chords upstream. Figure 6(b) shows the same information as in Fig. 6(a) but for the lower turbulence level case of 10%. Again, it can be seen that the measured and predicted turbulent kinetic energy agrees well at this location.

A comparison between the measured and predicted normalized turbulent kinetic energy and dissipation rate approaching the vane stagnation are illustrated in Figs. 7(a) and 7(b) for the 19.5% turbulence case. Although the initial conditions specified for the turbulence models at one chord upstream are higher than at the 0.33 chord location, the majority of the reduction occurs well

Table 2 Measured and predicted inlet turbulence conditions

	$X/C=-1$	$X/C=-0.33$
Measured 10% inset	No optical access	$k/U_{\text{inlet}}^2=0.015$ $\varepsilon C/U_{\text{inlet}}^3=0.0098$
Predicted 10% inlet	$k/U_{\text{inlet}}^2=0.026$ $\varepsilon C/U_{\text{inlet}}^3=0.027$	$k/U_{\text{inlet}}^2=0.015$ $\varepsilon C/U_{\text{inlet}}^3=0.0098$
Measured inlet 19.5%	No optical access	$k/U_{\text{inlet}}^2=0.0584$ $\varepsilon C/U_{\text{inlet}}^3=0.0519$
Predicted 19.5% inlet	$k/U_{\text{inlet}}^2=0.134$ $\varepsilon C/U_{\text{inlet}}^3=0.245$	$k/U_{\text{inlet}}^2=0.0584$ $\varepsilon C/U_{\text{inlet}}^3=0.0519$

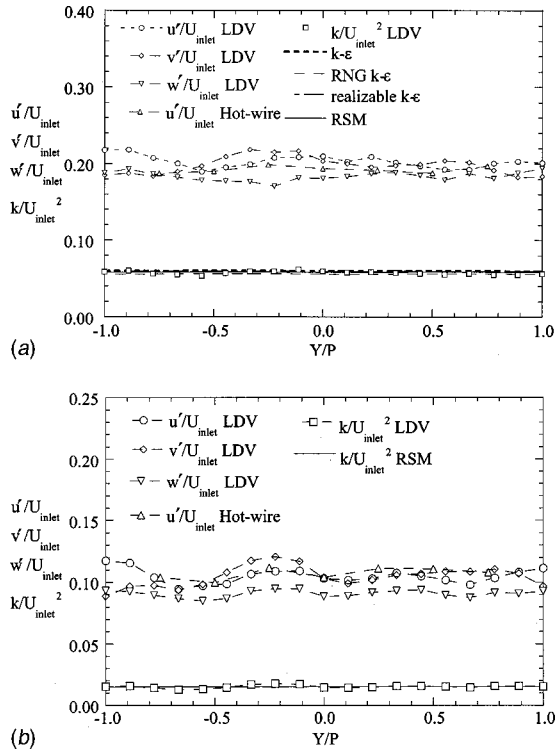

Fig. 6 (a) RMS levels of the velocity fluctuations in addition to the computed and predicted normalized turbulent kinetic energy distribution, k/U_{inlet}^2, at the inlet to the test section at $X/C=-0.33$ for the 19.5% case; (b) RMS levels of the velocity fluctuations in addition to the computed and predicted normalized turbulent kinetic energy distribution, k/U_{inlet}^2, at the inlet to the test section at $X/C=-0.33$ for the 10% case

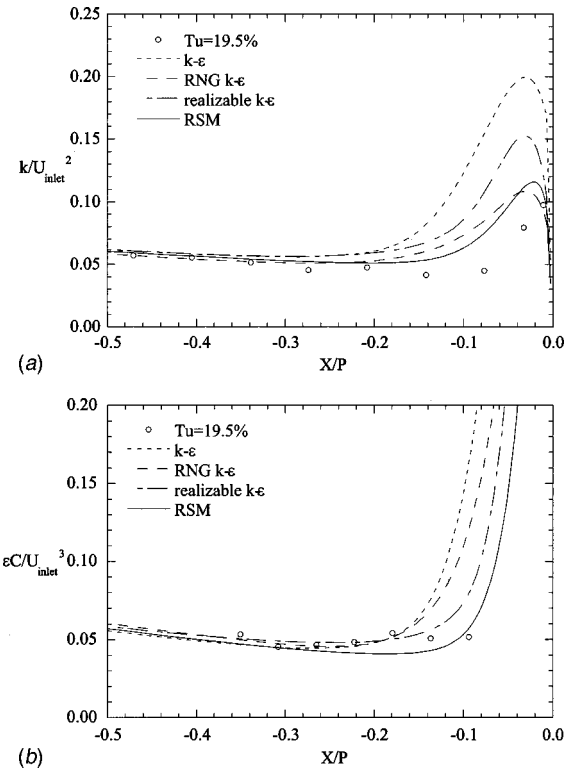

Fig. 7 (a) Comparison of measured and predicted normalized turbulent kinetic energy, k/U_{inlet}^2, approaching the vane stagnation for the 19.5% case; (b) comparison of measured and predicted dissipation rate, $\varepsilon C/U_{\text{inlet}}^3$, approaching the vane stagnation for the 19.5% case

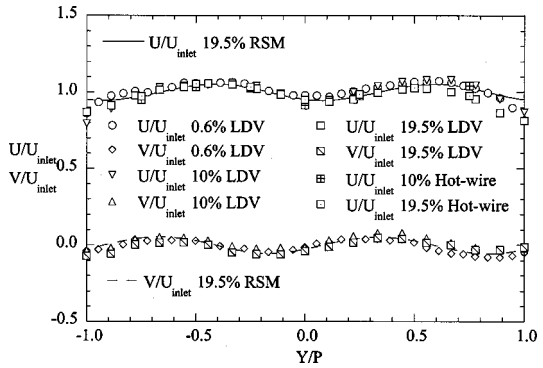

Fig. 8 Profiles of normalized streamwise, U/U_{inlet}, and pitchwise, V/U_{inlet}, velocity at the inlet to the test section at $X/C = -0.33$

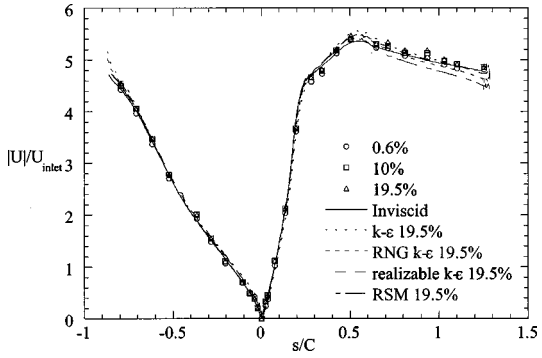

Fig. 9 Measured and predicted normalized freestream velocity, $|U|/U_{inlet}$, around the vane at several turbulence levels

upstream of the test section. At 0.33 chords, both the turbulent kinetic energy and dissipation rate are relatively flat but increase when approaching the vane. Note that the dissipation rates are only reported up to $X/P = -0.2$ because the velocity is quickly decreasing and the turbulence levels are very high making the hot-wire measurements invalid. All four turbulence models predict a rapid increase in the turbulent kinetic energy, but with varying peak levels. The RNG k-ε and Reynolds stress turbulence models predict more realistic peaks when comparing with the experimental measurements. Both experimental measurements and predictions show that the dissipation rate is essentially constant up to $X/P = -0.2$. Closer to the stagnation point, all four turbulence models overpredict the kinetic energy and predict a dramatic increase in the dissipation rate.

Figure 8 shows the streamwise and pitchwise mean velocity profiles at low and high freestream turbulence levels across the two flow passages around the central vane. Even though the generated turbulence levels from the active-grid are very high, the mean flowfield is unaffected. Figure 8 also shows the predicted mean velocity profiles using the Reynolds stress model. Although not shown, at this streamwise location, all of the turbulence models agree well with each other and the experimental measurements. Near the edges of the test section, the measurements deviate slightly from the predictions due to the development of boundary layers on the sides of the test section. This measurement location is upstream of a suction slot that is designed to remove the upstream boundary layer. Figures 6–8 show that at the inlet, good agreement has been achieved for both the mean and turbulent conditions between the experiment and CFD simulations. The following sections will discuss the results for the highly turbulent flowfield in the core region surrounding the stator vane.

Comparison of Experimental Data With Predictions From the Turbulence Models

The inviscid velocity distribution around the vane surface, calculated from the total and local static pressure measurements, as compared with the inviscid and viscous predictions is given in Fig. 9. The measured distribution on the pressure surface ($s/C < 0$) agrees well with the inviscid prediction as well as on the suction surface ($s/C > 0$) indicating that the outer wall placement was correct. The only difference between the inviscid and viscous predictions occurs on the trailing edge of the suction side with the viscous models predicting slightly lower velocities than observed in the measurements. This can be attributed to the flow slowing down in the wake region for the viscous cases whereas in the inviscid simulations, no wake occurs.

Figures 10(a)–(d) compare the normalized total velocity contours between experimental measurements at 0.6% and 19.5% and the CFD predictions at the 19.5% turbulence level. The flowfield measurements were performed between the mid-pitch of the two passages surrounding the central vane. To allow for an easier comparison with predictions, the pitch (Y/P) position for the data was numerically shifted to show contour levels between two adjacent vane stagnation points. The smoothness of these contours indicates the good periodicity between the two passages. The measured total velocity contours at an inlet turbulence level of 19.5% (Fig. 10(b)) is similar to that of the low inlet turbulence condition (Fig. 10(a)) with the exception that there is a larger high speed region on the suction side of the airfoil for the high turbulence. This larger high speed region is due to the transition of the boundary layer occurring earlier when the turbulence level is higher causing a thickening of the boundary layer and a higher speed inviscid region. Figures 10(c) and 10(d) show total velocity contours for the k-ε and Reynolds stress models for the 19.5% case. The total velocity contours for the RNG k-ε and realizable k-ε models are very similar to that of the k-ε model predictions. All four turbulence models predict the low speed region near the stagnation region as well as the acceleration as the flow enters the

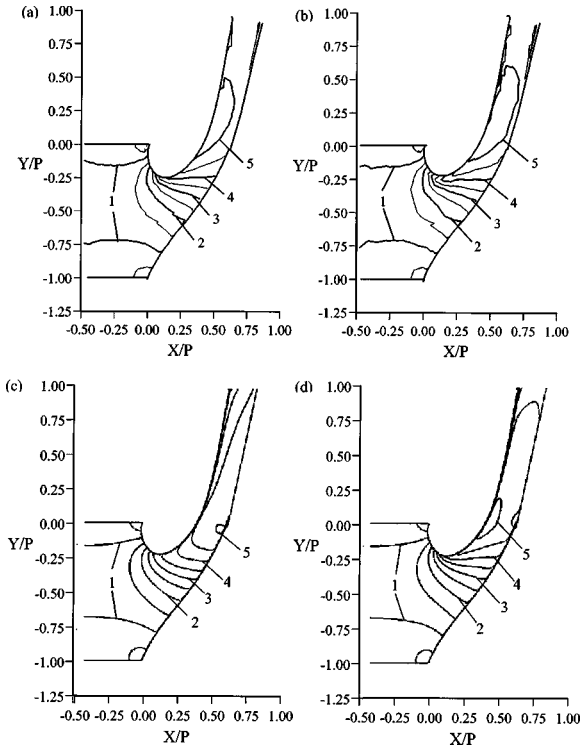

Fig. 10 Comparison of normalized total velocity, $|U|/U_{inlet}$, contours between (*a*) 0.6% experiment, (*b*) 19.5% experiment, (*c*) 19.5% k-ε, and (*d*) 19.5% RSM

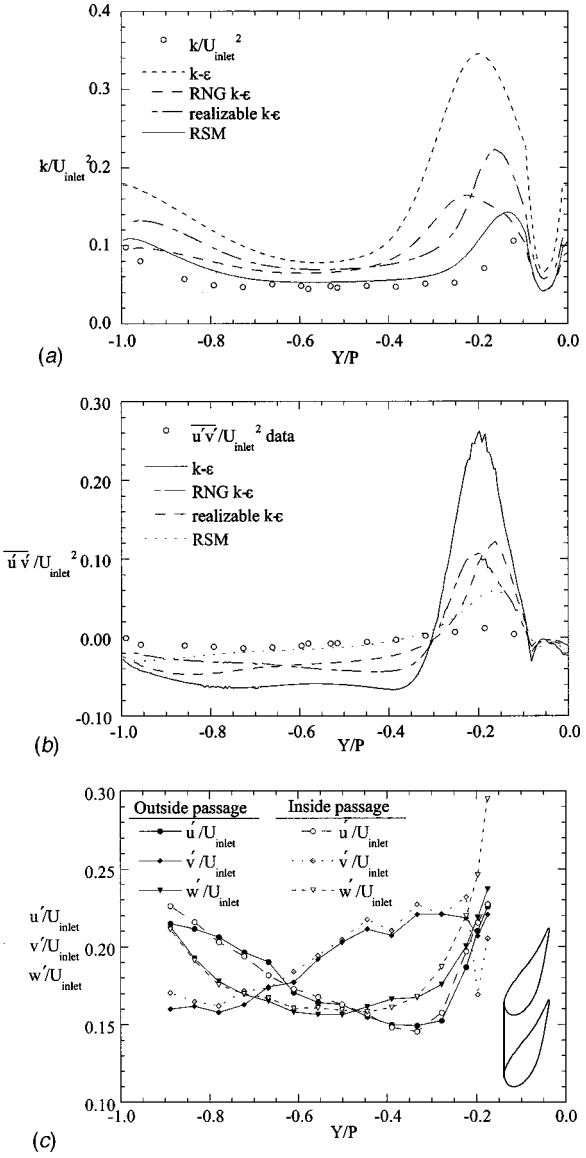

Fig. 11 (*a*) Normalized turbulent kinetic energy, k/U^2_{inlet}, at a line at the geometrical stagnation for the 19.5% case; (*b*) normalized Reynolds shear stress, $\overline{u'v'}/U^2_{inlet}$, at a line at the geometrical stagnation for the 19.5% case; (*c*) comparison of streamwise, u'/U_{inlet}, pitchwise, v'/U_{inlet}, and spanwise, w'/U_{inlet}, turbulence levels at a line between geometrical stagnation points for the 19.5% case

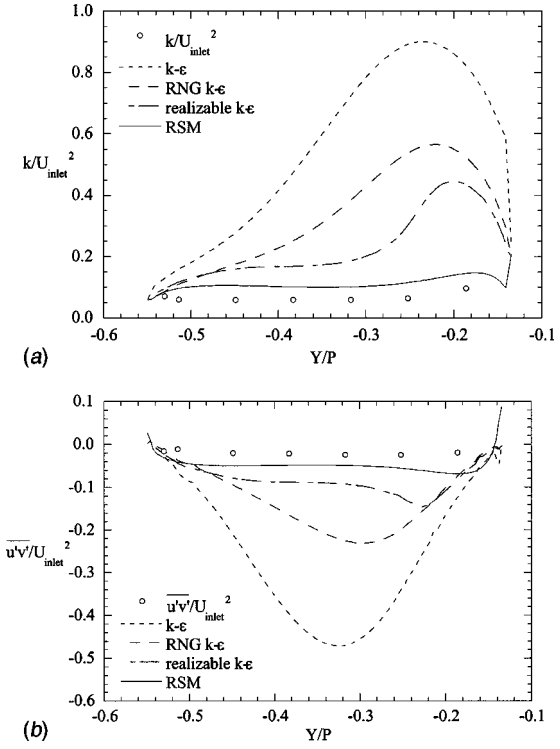

Fig. 12 (*a*) Comparison between measured and predicted normalized turbulent kinetic energy, k/U^2_{inlet}, at $X/P=0.295$ for the 19.5% case; (*b*) comparison between measured and predicted normalized Reynolds shear stress, $\overline{u'v'}/U^2_{inlet}$, at $X/P=0.295$ for the 19.5% case

passage. Downstream of the vane shoulder, however, the three eddy viscosity models predict that the high speed fluid moves away from the suction side of the vane. In the experimental measurements, as well as the Reynolds stress model, the highest speed fluid remains adjacent to the suction side of the vane.

Figures 11(*a*)–11(*b*) compare normalized turbulent kinetic energy (k/U_{inlet^2}) and Reynolds shear stress ($\overline{u'v'}/U_{inlet^2}$) across the pitch at the geometrical stagnation location ($X/P=-0.011$). The geometrical stagnation location is the farthest upstream axial position of the vane. At this location, the Reynolds stress model adequately predicts the levels of turbulent kinetic energy in the center of the passage whereas the eddy viscosity models greatly overpredict the levels. Similar to the curved channel, there is an overprediction of the turbulent kinetic energy near the surfaces of the turbine vanes ($Y/P\sim-1$ and -0.2) due to the acceleration along the pressure side. Although it is not shown here, the predictions for the low freestream turbulence case of 0.6% indicated very high turbulence levels for the *k*-ε and the RNG *k*-ε models. These high levels of turbulence result from the high straining rates and are in disagreement with the experimental measurements for the 0.6% turbulence case. As discussed previously, the *k*-ε and the RNG *k*-ε eddy viscosity models use a Boussinesq approximation for calculating the normal stresses from the turbulent kinetic energy. This approximation gave negative values of the streamwise normal stresses ($\overline{u'^2}$) because of the high turbulent viscosity and high strain rates. These unrealistic values demonstrate the limitations of the standard *k*-ε and RNG *k*-ε models for turbomachinery flows. The realizable *k*-ε model, developed to insure positive values for the Reynolds stresses, performed only slightly better than the other eddy viscosity models. The Reynolds stress model overpredicts the peak in the turbulent kinetic energy by approximately 20%.

Figure 11(*b*) compares measured and predicted normalized Reynolds shear stresses ($\overline{u'v'}/U_{inlet^2}$) across the pitch at the geometrical stagnation location. All four models overpredict the region of positive shear stress near the suction surface ($Y/P=-0.2$), with the standard *k*-ε model showing the largest disagreement with the measurements and the Reynolds stress model showing the closest agreement with the measured values. The three eddy viscosity models predict negative shear stress values in the middle of the passage where the experiments and Reynolds stress model show very low positive values of $\overline{u'v'}/U_{inlet^2}$.

Figure 11(*c*) shows the measured normalized rms levels of the streamwise, u'/U_{inlet}, pitchwise, v'/U_{inlet}, and spanwise, w'/U_{inlet}, fluctuating velocities at the geometrical stagnation point for the 19.5% turbulence case. At this location, the strong flow acceleration has caused considerable anisotropy in the rms levels of the fluctuating velocities. The streamwise acceleration near the suction surface causes a decrease in the streamwise fluc-

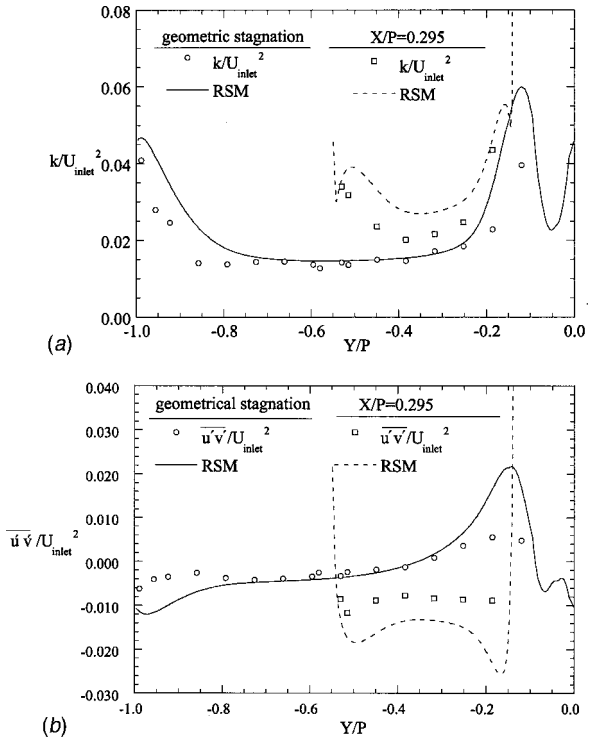

Fig. 13 (*a*) Comparison between measured and predicted normalized turbulent kinetic energy, k/U^2_{inlet}, at the geometric stagnation and $X/P=0.295$ for the 10% case; (*b*) comparison between measured and predicted Reynolds shear stress, $\overline{u'v'}/U^2_{inlet}$, at the geometric stagnation and $X/P=0.295$ for the 10% case

tuations. A redistribution of the turbulent energy results in increase in the pitchwise fluctuations at the same location. An increase in the spanwise fluctuations is observed near the vane surfaces.

Figures 12(*a*) and 12(*b*) show the comparisons of turbulent kinetic energy and shear stress at a location of $X/P=0.295$ for the 19.5% case. Again, the Reynolds stress model provides the best agreement with the measurements. As in Figs. 11(*a*)–11(*b*), all of the eddy viscosity models greatly overpredict the magnitude of the turbulent kinetic energy and Reynolds shear stress.

A comparison of the measured and predicted turbulent kinetic energy, k/U_{inlet^2}, and Reynolds shear stress, $\overline{u'v'}/U_{inlet^2}$, for the 10% case at the vane geometric stagnation location ($X/P=-0.011$) and at $X/P=0.295$ are shown in Figs. 13(*a*) and 13(*b*). As with the 19.5% case, good agreement with experimental measurements is observed in the middle of the passage at the geometrical stagnation point. The Reynolds stress model slightly overpredicts the turbulent kinetic energy and Reynolds shear stress near the vane surface. Farther into the vane passage, the Reynolds stress model overpredicts the magnitude of both the turbulent kinetic energy and Reynolds shear stress. However, the agreement between computation and experiment is better for the 10% case than it was for the 19.5% case.

Comparison of 10% and 19.5% Turbulence Levels

Examination of Figs. 11–13 show that all of the eddy viscosity models (k-ε, RNG k-ε, and the realizable k-ε) overpredict the turbulent kinetic energy and Reynolds shear stress. The largest overprediction occurs near the convexly-curved suction surface of the airfoil, similar to the overpredictions for the convexly-curved wall for the U-duct simulations. It is also evident that the Reynolds stress model provides much better agreement with the experimental measurements than either of the eddy viscosity models.

Figures 14(*a*)–14(*d*) compare the measured and predicted normalized Reynolds shear stress, $\overline{u'v'}/U^2_{inlet}$, for the 10% and 19.5%, respectively. Comparison of the experimental measurements and predictions at the different inlet turbulence levels show that although the magnitudes are different, the sign of the Reynolds stress are in agreement. Positive values of the Reynolds shear stress are found near the geometrical stagnation location on the suction side of the vane, while negative values of shear stress occur further downstream in the passage center. The lower turbulence level of 10% has much lower values of the Reynolds stress as compared to the 19.5% case. The lower values of Reynolds stress can be explained by examining the production term for $\overline{u'v'}$ given as

$$P(\overline{u'v'})=u'^2\left(-\rho\frac{\partial V}{\partial X}\right)+v'^2\left(-\rho\frac{\partial U}{\partial Y}\right) \tag{5}$$

Equation (5) shows that for this two-dimensional flowfield the production of the Reynolds shear stress has two terms that are functions of mean velocity gradients and normal stresses. The nearly identical mean flowfield between the 10% and 19.5% cases indicate that the derivates of the velocity field should be nearly identical. Thus, the difference in production between these two cases is caused by different magnitudes of the velocity fluctuations. Equation (5) shows that the lower turbulence levels will result in less production of Reynolds shear stress for the lower turbulence condition. Both terms in Eq. (5), indicate that near the geometrical stagnation point on the suction side of the vane, production of positive Reynolds stress occurs due to the flow turning down and around the suction surface. Moving into the passage, both terms in Eq. (5) show that negative Reynolds stress will be produced as the flow is being turned up through the passage. Near the trailing edge of the vane, only small mean velocity gradients

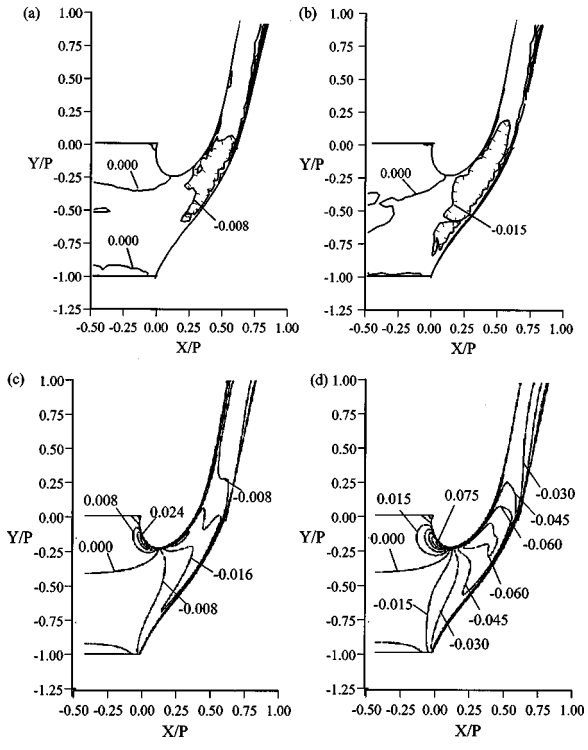

Fig. 14 Comparison of normalized Reynolds shear stress contours, $\overline{u'v'}/U^2_{inlet}$, between (*a*) 10% experiment, (*b*) 19.5% experiment, (*c*) 10% RSM, and (*d*) 19.5% RSM

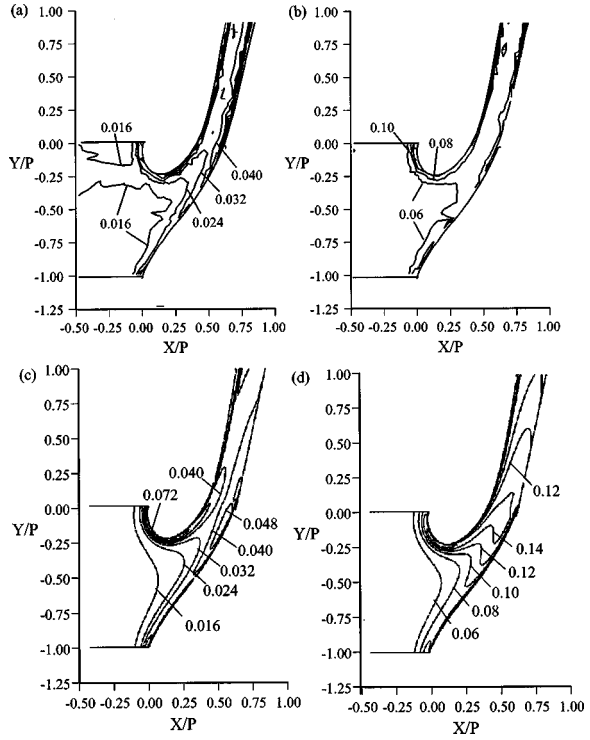

Fig. 15 Comparison of normalized turbulent kinetic energy contours, k/U^2_{inlet}, between (*a*) 10% experiment, (*b*) 19.5% experiment, (*c*) 10% RSM, and (*d*) 19.5% RSM

exist and the production of Reynolds shear stress reduces to zero. The Reynolds stress model predictions, shown in Figs. 14(*c*) and 14(*d*), indicate the same sign but larger magnitudes as compared with the experiments for both the 10% and 19.5% cases.

Figures 15(*a*)–15(*d*) compare the normalized turbulent kinetic, k/U_{inlet^2}, between experimental measurements and the Reynolds stress model predictions at 10% and 19.5%, respectively. Significant differences exist between the development of the turbulent kinetic energy at the different turbulence levels. The experimental measurements for the 19.5% case show that the turbulent kinetic energy levels increase by as much as 31% in the vane passage. At the lower inlet turbulence level of 10%, the turbulent kinetic energy through the passage increases by 130%, which is significantly higher than for the 19.5% case. Although the turbulent kinetic energy is significantly increasing through the passage, it is important to recognize that the mean velocity has accelerated up to five times the inlet velocity. This means that the turbulence level at the passage exit has decreased to approximately 3% for the 10% inlet turbulence case and 6% for the 19.5% inlet turbulence case.

The difference in the measured turbulent kinetic energy contours between the two turbulence levels can be explained by examining the mechanism for turbulent kinetic energy production given as

$$P(k)=u^2_{\text{rms}}\left(-\rho\frac{\partial U}{\partial X}\right)+\overline{u'v'}\left(-\rho\frac{\partial U}{\partial Y}-\rho\frac{\partial V}{\partial X}\right)+v^2_{\text{rms}}\left(-\rho\frac{\partial V}{\partial Y}\right) \tag{6}$$

As a result of the identical mean flow field and geometry, the ratio of turbulent kinetic energy production between the two high turbulence cases can be examined by comparing the measured Reynolds stresses. The gradients in Eq. (6) were evaluated from the CFD solution, which is a reasonable assumption given the good agreement between measurements and predictions, at locations where direct measurements of the Reynolds stresses were taken. The CFD solution was used because of the higher resolution

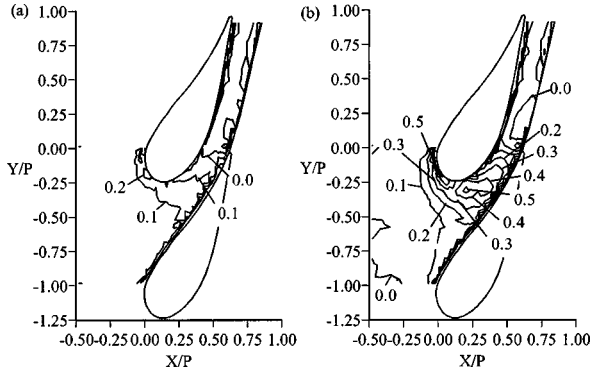

Fig. 16 Comparison of normalized turbulent kinetic energy production, $P(k)C/\rho U^3_{\text{inlet}}$, contours between (*a*) 10% experiment and (*b*) 19.5% experiment

thereby giving more accurate gradients than the experimental measurements. Figures 16(*a*) and 16(*b*) show contours of turbulent kinetic energy production for the 10% and 19.5% using the CFD mean velocities and the measured Reynolds stresses. For both these cases the largest production occurs near the shoulder of the vane passage in the high acceleration region. Over the majority of the flowfield, the 19.5% case has nearly three times the production as compared to the 10% case. The measurements indicate, however, that the 19.5% case has only a 31% increase in the turbulent kinetic energy through the vane passage, while the 10% case has a much larger increase at 131%. This difference can be explained by the fact that the dissipation at the inlet for the 19.5% case was about six times that for the 10% case. The higher value of the dissipation appears to counteract the higher production rates causing only a slight rise in the turbulent kinetic energy in the vane passage for the 19.5% case as compared to the 10% case.

The Reynolds stress model predictions shown in Fig. 15(*d*) for the 19.5% case give an overprediction of the turbulent kinetic energy in the vane passage by as much as 125%. At the lower turbulence level of 10%, shown in Fig. 15(*c*), the turbulent kinetic energy in the passage is overpredicted by only 25%. The Reynolds stress model predictions indicate a 160% and 125% increase in turbulent kinetic energy through the vane passage as compared to the measured 130% and 31% increase for the 10% and 19.5% cases, respectively.

Although the Reynolds stress model performed better than the eddy viscosity models, the levels of turbulent kinetic energy and shear stress were overpredicted. One possible explanation is that the Reynolds stress model used in this investigation used the same transport equation for the dissipation rate as the standard k-ε model. The limitations of this transport equation for the dissipation rate have been discussed in Lou and Lakshminarayana [26] and Shih et al. [19]. In this transport equation, the production of dissipation is set equal to the production of turbulent kinetic energy. Figures 17(*a*) and 17(*b*) show contours of a normalized dissipation rate for the 19.5% turbulence case. In the transport equation for the dissipation rate used in the realizable k-ε model, the production of dissipation is proportional to the mean strain rate of the flow. Comparisons of dissipation contours between the realizable k-ε and Reynolds stress model showed that the Reynolds stress model had dissipation levels much less than the realizable k-ε prediction. The use of a different transport equation for the dissipation rate, such as the one used in the realizable k-ε model, could produce better agreement with the experimental measurements.

Another possible reason for the over prediction of the turbulent kinetic energy involves the constants used in the RSM. These constants were evaluated for flows not too far removed from simple shear flows. The validity of these constants for flows with

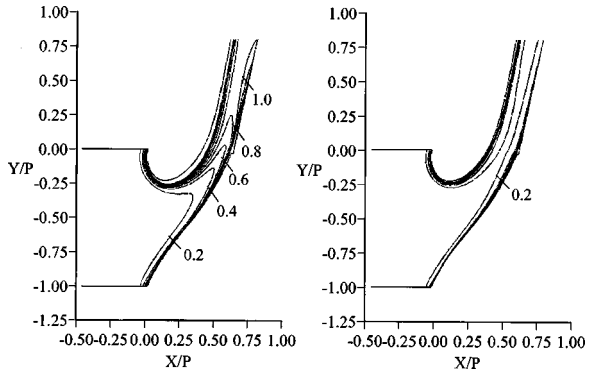

Fig. 17 Comparison of normalized dissipation rates, $\varepsilon C/U_{inlet}^3$, at 19.5% between (*a*) realizable *k*-ε model and (*b*) RSM

high freestream strain rates at elevated turbulence levels is not known. Supporting this reason is the fact that the results from the 10% case do indicate much better agreement with the measurements than the 19.5% case.

Conclusions

Experimental measurements in a stator vane passage at high freestream turbulence levels of 10% and 19.5% were compared to RANS predictions using a variety of turbulence models. The experimental measurements indicated increases in the turbulent kinetic energy of the flow as the flow convected through the turbine vane passage with much larger increases for the 10% turbulence case as compared with the 19.5% case. This difference was attributed to the fact that the dissipation was much higher for the 19.5% case.

The eddy viscosity models greatly overpredicted the turbulent kinetic energy in the vane passage as a result of the overproduction of turbulent kinetic energy in the high acceleration region resulting in additional strain. On the suction side of the airfoil where the surface is convex, the standard *k*-ε and RNG *k*-ε model produced physically unrealistic negative values for the streamwise normal stresses. The realizable *k*-ε model, developed to insure positive values of the normal stresses, performed slightly better than the other eddy viscosity models. The Reynolds stress model provided the best agreement with the experimental measurements; however, the Reynolds stress model overpredicted the turbulent kinetic energy by 125% for the 19.5% case. Considerably better agreement was achieved between measurements and predictions for the lower turbulence case of 10%. At this turbulence level, the Reynolds stress model overpredicted the turbulent kinetic energy by only 25%.

The relatively poor predictions, particularly at the high turbulence levels, may be the result of several issues. First, the current transport equation in the RSM gave very low values for the dissipation rate in the vane passage as compared to the realizable *k*-ε model. The use of a Reynolds stress model with an improved transport equation for the dissipation rate, such as the one used in the realizable *k*-ε model, may give results closer to the experimental measurements. Second, the constants used in the RSM model were evaluated from simple shear flows not too far removed from equilibrium. The better agreement for the 10% case as compared with the 19.5% case supports this reasoning.

Acknowledgments

The authors would like to thank the Department of Energy's Advanced Gas Turbine Systems Research Program for supporting this work and Dr. Lawrence Golan for serving as the contract monitor. The authors would also like to thank Pratt & Whitney, Florida for supplying the turbine vane geometry and the National Science Foundation (CTS-9996224) for their support.

Nomenclature

C = true chord length
$E_1(\kappa_1)$ = spectra for streamwise fluctuations
f = frequency
k = turbulent kinetic energy, $k=0.5(u'^2+v'^2+w'^2)$
n = distance normal to the convex curved surface
P = turbine vane pitch
R = radius of curvature for a streamline
rms = root-mean-square of the fluctuations
Re_{in} = Reynolds number based on chord length and incident velocity
S = freestream strain rate
U_{inlet} = upstream incident velocity
$\overline{u'v'}$ = Reynolds shear stress
u, v, w = local mean velocities along a streamline
U, u' = mean and rms of fluctuating velocity in the *X*-direction
V, v' = mean and rms of fluctuating velocity in the *Y*-direction
w' = rms of fluctuating velocity in the *Z*-direction
W = passage width for the curved channel simulation
X = fixed coordinate parallel with the inlet flow where origin is at the flow stagnation
Y = fixed coordinate in the cross-pitch direction
Z = fixed coordinate in the spanwise direction
ε = turbulent dissipation obtained from Eq. (1)
κ_1 = wavenumber, $\kappa_1=2\pi f/U$
Λ_x = streamwise integral length scale
λ = Taylor microscale
ν = kinematic viscosity
σ = Stefan-Boltzman constant
η = timescale ratio

References

[1] Ames, F. E., 1995, ''The Influence of Large-Scale High-Intensity Turbulence on Vane Heat Transfer,'' ASME J. Turbomach., **119**, pp. 23–30.
[2] Radomsky, R. W., and Thole, K. A., 1998, ''Effects Of High Freestream Turbulence Levels and Length Scales on Stator Vane Heat Transfer,'' ASME Paper No. 98-GT-236.
[3] Goldstein, R. J., Lau, K. Y., and Leung, C. C., 1983, ''Velocity and Turbulence Measurements in Combustion Systems,'' Exp. Fluids, **1**, pp. 93–99.
[4] Bradshaw, P., 1973, ''Effects of Streamline Curvature on Turbulent Flow,'' AGARDograph 169.
[5] Launder, B. E., Reece, J. C., and Rodi, W., 1975, ''Progress in the development of a Reynolds-stress Turbulence Closure,'' J. Fluid Mech., **68**, pp. 537–566.
[6] Durbin, P. A., and Speziale, C. G., 1991, ''Local Anisotropy in Strained Turbulence at High Reynolds Numbers,'' ASME J. Fluids Eng., **113**, pp. 707–709.
[7] Lakshminarayana, B., 1991, ''An Assessment of Computational Fluid Dynamic Techniques in the Analysis and Design of Turbomachinery-The 1990 Freeman Scholar Lecture,'' ASME J. Fluids Eng., **113**, pp. 315–352.
[8] Luo, J., and Lakshminarayana, B., 1997, ''Prediction of Strongly Curved Turbulent Duct Flows with Reynolds Stress Model,'' AIAA J., **35**, No. 1, pp. 91–98.
[9] Kang, M., Kohli, A., and Thole, K. A., 1999, ''Heat Transfer and Flowfield Measurements in the Leading Edge Region of a Stator Vane Endwall,'' ASME J. Turbomach., **121**, No. 3, pp. 558–568.
[10] Kang, B., and Thole, K. A., 1999, ''Flowfield Measurements in the Endwall Region of a Stator Vane,'' ASME J. Turbomach., **122**, pp. 458–466.
[11] Radomsky, R. W., and Thole, K. A., 1999, ''Flowfield Measurements for a Highly Turbulent Flow in a Stator Vane Passage,'' accepted for ASME J. Turbomach.
[12] Bangert, B., Kohli, A., Sauer, J., and Thole, K. A., 1997, ''High Freestream Turbulence Simulation in a Scaled-Up Turbine Vane Passage,'' ASME Paper No. 97-GT-51.
[13] Moffat, R. J., 1998, ''Describing Uncertainties in Experimental Results,'' Experimental and Fluid Science, **1**, pp. 3–17.
[14] Patankar, S. V., 1980, *Numerical Heat Transfer and Fluid Flow*, Hemisphere, Washington D.C.
[15] FLUENT User's Guide, 1998, Release 5.0, Fluent Inc., Lebanon, N. H.
[16] Kim, S. E., and Choudhury, D., 1995, ''A Near-Wall Treatment Using Wall Functions Sensitized to Pressure Gradient,'' ASME FED Vol. 217, Separated and Complex Flows, ASME.
[17] Launder, B. E., and Spalding, D. B., 1974, ''The Numerical Computation of

Turbulent Flows,'' Comput. Methods Appl. Mech. Eng., **3**, pp. 269–289.
[18] Yakhot, V., and Orszag, S. A., 1992, ''Development of Turbulence Models for Shear Flows by a Double Expansion Technique,'' Phys. Fluids A, **4**, No. 7, pp. 1510–1520.
[19] Shih, T. H., Liou, W. W., Shabbir, A., Yang, Z., and Zhu, J., 1995, ''A New k-ε Eddy Viscosity Model for High Reynolds Number Turbulent Flows,'' Comput. Fluids, **24**, No. 3, pp. 227–238.
[20] Lien, F. S., and Leschziner, M. A., 1994, ''Assessment of Turbulent Transport Models Including Non-Linear RNG Eddy Viscosity Formulation and Second-Moment Closure for Flow Over a Backward-Facing Step,'' Comput. Fluids, **23**, No. 8, pp. 983–1004.
[21] Speziale, C. G., Sarkar, S., and Gatski, T. B., 1991, ''Modelling the Pressure-Strain Correlation of Turbulence: An Invariant Dynamical Systems Approach,'' J. Fluid Mech., **227**, pp. 245–272.
[22] Monson, D. J., and Seegmiller, H. L., 1992, ''An Experimental Investigation of Subsonic Flow in a Two-Dimensional U-duct,'' NASA Contract Report 103931.
[23] Wolfstein, M., 1969, ''The Velocity and Temperature Distribution of One-Dimensional Flow with Turbulence Augmentation and Pressure Gradient,'' Int. J. Heat Mass Trans., **12**, pp. 301–318.
[24] Mayle, R. E., Dullenkopf, K., Schulz, A., 1998, ''The Turbulence That Matters,'' ASME J. Turbomach., **114**, pp. 707–714.
[25] Hinze, J., 1975, *Turbulence*, 2nd Edition, McGraw-Hill, New York.
[26] Luo, J., and Lakshminarayana, B., 1997, ''Analysis of Streamline Curvature Effects on Wall-Bounded Turbulent Flows,'' AIAA J., **35**, No. 8, pp. 1273–1279.
[27] Gibson, M. M., and Rodi, W., 1981, ''A Reynolds-Stress Closure Model of Turbulence Applied to the Calculation of a Highly Curved Mixing Layer,'' J. Fluid Mech., **103**, pp. 161–182.